

New Insight into Li⁺ Dynamics in Lithium Bimetal Phosphate

Laurence Savignac¹, John M. Griffin^{2,3}, Steen B. Schougaard^{1z}

Affiliation(s):

¹NanoQAM and the department of chemistry, Université du Québec à Montréal, Case postale 8888 Succ. Centre-ville, Montréal, Qc, Canada, H3C 3P8

²Department of Chemistry, Lancaster University, Lancaster, LA1 4YB, UK

³Materials Science Institute, Lancaster University, Lancaster, LA1 4YB, UK

^zCorresponding Author E-mail Address [schougaard.steen@uqam.ca]

Abstract

Substitution of iron by other transition metals within the remarkably stable *olivine* framework is of interest considering the expected gain in energy density. However, manganese rich *olivine* materials suffer from sluggish redox kinetics, leading to electrochemical performances at high current densities which are below expectations. The source of the kinetic limitations is not clear, with multiple processes having been proposed, including low bulk electronic conductivity, structural instability of Mn³⁺ and a phase transition mechanism. This study employed ⁷Li MAS NMR relaxation techniques to indirectly probe Li⁺ dynamics using various stoichiometry of chemically prepared Li_xMn_yFe_{1-y}PO₄ (0 ≤ (x, y) ≤ 1). Focusing on the particle level, the aim was to understand how the different crystal phases, alongside the Mn structural contribution, influence Li⁺ transport at each stage of the oxidation process. Significantly, the formation of an *olivine* solid solution with vacancies within this progression gave rise to a faster ⁷Li transverse relaxation derived from superior Li⁺ motion.

Introduction

LiFePO₄ is recognized for its outstanding structural stability, which is derived from the strong P-O bond, and which is reflected in its excellent capacity retention.¹ The flat plateau signature on galvanostatic charge and discharge curves reflects a two-phase equilibrium during the vast majority of the process (0.02 ≤ x ≤ 0.95).² Despite the perception that translation of the interface caused by the structural mismatch between LiFePO₄ and FePO₄ could be kinetically limiting, a previous study showed that complete delithiation can be reached in ~10s following a two-phase path.³

The desire to incorporate high voltage transition metals to benefit from *olivine*'s attributes is commercially relevant, as it increases energy density. Manganese is here an ideal candidate due to its abundance and low cost *i.e.* LiMnPO₄ has potentially 20% higher energy density than LiFePO₄ if theoretical capacity is reached.⁴ Nevertheless, Mn-rich *olivine* still exhibit sluggish kinetics⁵⁻⁷ which may be linked to : i) instability of MnPO₄⁸ ii) Jahn-Teller distortion⁹ and iii) large ionic radii difference between Mn²⁺-Mn³⁺ amplifying structural mismatch¹⁰. Conversely, doping *olivine* LiFePO₄ with Mn has shown improved cyclic stability compared to LiMnPO₄.¹¹ Moreover, at intermediate Mn substitution levels, a transient solid solution formed during charge/discharge seems to improve ionic and electronic conductivity throughout the processes¹² along with limiting structural mismatch¹³ of the end structures during the transitory solid solution.

The analysis of the phases formation during the delithiation is complex due to the

substantial influence of synthesis conditions and the choice of equilibrium *vs* dynamic probing method.^{14, 15} From chemically oxidized materials, Yamada *et al.*¹⁶ have characterized multiple $\text{Li}_x\text{Mn}_y\text{Fe}_{1-y}\text{PO}_4$ compositions using X-ray diffraction (XRD) and X-ray absorption fine structure (EXAFS). The resulting two-dimensional phase diagram displays crystalline phases at different state of oxidation with a noted instability for the Mn rich structure. Besides, Perea *et al.*¹⁷ have carried out *operando* XRD and ^{57}Fe Mössbauer spectroscopy on electrochemically cycled $\text{Li}_x\text{Mn}_y\text{Fe}_{1-y}\text{PO}_4$ exhibiting distinctives two-phases processes for $\text{Fe}^{2+}/\text{Fe}^{3+}$ and $\text{Mn}^{2+}/\text{Mn}^{3+}$ redox sites. Major discrepancies of the solid solution range are reported from these two experiments along with studies on single $\text{Li}_x\text{Mn}_y\text{Fe}_{1-y}\text{PO}_4$ composition.^{14, 15, 18-25}

On Li^+ dynamics probing in *olivines*, Liu *et al.*²⁶ have developed an exchange experiment that employed ^6Li and ^7Li NMR to reveal the consequence of anti-site defects on Li^+ diffusion in LiFePO_4 particles. The sensitivity of NMR on Li^+ dynamics motivate its use for $\text{Li}_x\text{Mn}_y\text{Fe}_{1-y}\text{PO}_4$ with the aim of adapting a method suitable for multiple Mn sample composition analysis.

To better understand the complex mechanism in play of the dual redox site material, $\text{Li}_x\text{Mn}_y\text{Fe}_{1-y}\text{PO}_4$ ($0 \leq (x, y) \leq 1$) samples were characterized by complementary methods: i) XRD to obtain long-range the bulk crystalline structures, ii) ^7Li magic angle spinning nuclear magnetic resonance spectroscopy (MAS NMR) to probe Li^+ local environment and iii) atomic emission spectroscopy (AES) and inductive coupled plasma emission spectroscopy (ICP-ES) for Li, Mn and Fe quantification. The chemical preparation of delithiated materials using $\text{Br}_{2(l)}$ (4.1V *vs* Li/Li^+)²⁷ was preferred to the equivalent electrochemical potentiometric method to avoid inhomogeneity due to unconnected particles as well as interference from other components in the composite electrode (carbon and polymer binder).

With these $\text{Li}_x\text{Mn}_y\text{Fe}_{1-y}\text{PO}_4$ materials in hand at strategic degrees of delithiation, the purpose of the following study was to indirectly probe Li^+ motion using transverse relaxation T_2 measurements. Recently implemented in the field of paramagnetic materials,²⁸ changes in T_2 parameter provides access to Li^+ dynamics information since relaxation of nuclei is highly dependent on motion at the atomic scale. Additionally, it paves the way for understanding facets of Li^+ transport in complex materials like $\text{LiMn}_y\text{Fe}_{1-y}\text{PO}_4$ and how these are impacted by the formation of an *olivine* solid solution with vacancies.

Experimental

Materials synthesis

$\text{LiMn}_y\text{Fe}_{1-y}\text{PO}_4$ ($y = 0.3, 0.5, 0.7$) powders were synthesized using solid state process. Lithium carbonate (Li_2CO_3 , Fisher Scientific, ACS grade), ammonium phosphate monobasic ($\text{NH}_4\text{H}_2\text{PO}_4$, Anachemia, 98%), manganese oxalate dihydrate ($\text{MnC}_2\text{O}_4 \cdot 2\text{H}_2\text{O}$, Alfa Aesar, 99.5%) and iron oxalate dihydrate ($\text{FeC}_2\text{O}_4 \cdot 2\text{H}_2\text{O}$, Sigma-Aldrich, 99 %) was used in stoichiometric ratios 0.52:1: y : $1-y$, respectively. A total reagents mass of 3.15 g was roll-milled using zirconia cylinders in 15 mL of acetone for 48h. The acetone was let to evaporate and the ground powder underwent a degassing process at 350°C for 3h under nitrogen flow. The roll-milling was repeated and the powder underwent a subsequent sintering at 600°C for 12h resulting in a highly crystalline product as per XRD.

Chemical oxidation

Various Li⁺ compositions (x) in Li _{x} Mn _{y} Fe_{1- y} PO₄ ($y = 0.3, 0.5, 0.7$) powders were obtained by mixing 0.2 g of LiMn _{y} Fe_{1- y} PO₄ with 10% molar excess of liquid bromine (Anachemia, ACS) for targeted x in 10 mL of acetonitrile (ACN, Sigma-Aldrich, 99.9 %). The reaction mixture was stirred and kept in the dark at 40°C for 7 days. The powder was recovered by vacuum filtration on a Büchner funnel, subsequently washed with 2*50 mL of ACN before drying overnight at 50 °C in vacuum.

Characterizations

The particle size distribution was estimated to 920-970 nm (SM Figure S1) using dynamic light scattering measurement (ZetaPlus, BrookHaven Instrument Corp.).

Li, Mn and Fe quantitative analysis was executed in triplicates. 9 mg of LFMP was dissolved in 20 mL of boiling concentrated nitric acid (Caledon), transferred to a 100 mL volumetric flask, and subsequently diluted 10/100 mL with 5 % HNO₃. The Li content of samples was confirmed by atomic emission spectroscopy (AES, Varian SpectrAA 220 FS at 670.8 nm) where a calibration curve (0.1–0.6 ppm) was made from Li standard solution (Alfa Aesar, Li₂CO₃ in 5% HNO₃). The Mn/P and Fe/P ratios were confirmed by inductive coupled plasma emission spectroscopy (ICP-ES, Thermo 6500 Dual View) where a calibration curve (0.1-5.0 ppm) was made from Mn, Fe and P 5 % in HNO₃ standard solutions (Fisher, SpectraPure and Alfa Aesar respectively). Confidence intervals were calculated at 95% confidence level using Student-t-statistics.

Powders were characterized by X-ray diffraction using a Phillips X'Pert Pro diffractometer with Cu K _{α} radiation (1.5418 Å). The current and voltage were 40 mA and 40 kV respectively with a step size of 0.015° s⁻¹ in the 2 θ range of 15–60°. 10 % m/m silicon powder 1–5 μ m (Alfa Aesar 99.5%) was mixed into the sample, as an internal standard. Rietveld refinement was performed Fullprof 3.2 software (SM Figure S2).²⁹

⁷Li MAS NMR experiments were performed using a 400 MHz Bruker Avance III HD WB spectrometer at a Larmor frequency of 155.467 MHz and a 9.4 T magnetic field strength. Ambient-temperature experiments were performed using a Bruker 1.9 mm probe at a MAS rate of 20 kHz. Spectra were referenced relative to 1 M LiCl solution (0 ppm). Spinning sidebands were identified by changing the MAS rate, *i.e.* 33.33 and 40 kHz, where a change in position indicated a rotation feature. For T₂ relaxation measurements, a Hahn echo pulse sequence was used with the echo delay τ , defined as the delay between 90 and 180° pulses midpoints, corresponding to one rotor period (50 μ s). The 90° pulse length was 2.5 μ s, and a recycle delay of 0.05 s was used. T₂ values (μ s) were obtained from a fitting process of the signal intensity vs τ using a single exponential equation in TopSpin 3.6.1 software (SM figure S5 and Eq. S1). For selected samples measured in triplicates, confidence intervals were calculated at 95% confidence level using Student-t-statistics. For T₁ relaxation measurements, an inversion-recovery pulse sequence was followed by a Hahn echo pulse sequence with the same pulse length and recycle delay as the T₂ experiment. Temperature-dependent T₂ measurements were performed using a Bruker 4.0 mm probe at a MAS rate of 15 kHz and an echo delay τ corresponding to one rotor period (66.67 μ s). In order to correct for frictional heating, the temperatures were calibrated at the same spinning frequency used for T₂ measurements using methanol.³⁰ A 15 min equilibration period was employed for temperature stabilization prior to measurement. The 90° pulse length was 2 μ s, and a recycle delay of

0.05 s was used.

Results and Discussion

The stoichiometry was measured directly using AES and ICP-ES (SM Table S1). Lithium values in excess of the stoichiometric $x = 1$, indicates that residual Li^+ is present in the pristine material, e.g. $\text{Li}_{1.11}\text{Mn}_{0.5}\text{Fe}_{0.5}\text{PO}_4$, due to the use of an excess of reagent during synthesis. The excess is necessary to ensure highly crystalline samples that follow Vegard's law over the whole Mn/Fe compositional range. This additional lithium is most likely present as impurity at the surface of the particle, e.g. Li_3PO_4 ³¹, in trace or amorphous quantities since no peaks are detectable in the diffractograms (Figure 1a).

The structural evolution of crystalline phases at various steps of delithiation was obtained from powder XRD for $\text{Li}_x\text{Mn}_{0.5}\text{Fe}_{0.5}\text{PO}_4$ (Figure 1a) and $\text{Li}_x\text{Mn}_{0.7}\text{Fe}_{0.3}\text{PO}_4$ (SM Figure S3) and is in agreement with previous literature²⁰. Analysis of the first sample, $\text{Li}_x\text{Mn}_{0.5}\text{Fe}_{0.5}\text{PO}_4$, will be described in detail in the following.

The XRD pattern of $\text{Li}_x\text{Mn}_{0.5}\text{Fe}_{0.5}\text{PO}_4$ delithiated by means of an excess of oxidant shows exclusively the *heterosite* phase (Figure 1a). The shifts of the peaks to higher angles, compared to the *heterosite* phase in other samples ($x = 0.50$ and $x = 0.55$), are interpreted as unit cell shrinkage associated with lithium removal as previously reported for the completely delithiated phase¹⁶. Possible traces of solid solution islands could be indicated by peak asymmetry and the 7 ± 2 % of Li^+ remaining within the structure originating from presence of anti-site defects blocking Li^+ channels²⁶. The two subsequent diffractograms with $x = 0.50$ and $x = 0.55$ (Figure 1a) displays a two-phase system composed of Li-rich *olivine* and Li-poor *heterosite* phases. For materials with a low degree of delithiation, i.e. when $x = 0.67$ and $x = 0.86$, only one phase is present suggesting that Li^+ is homogeneously distributed within the *olivine* structure (Figure 1a). The resulting phase intervals for the delithiation process are approximated as the following: *heterosite* for $0.00 \leq x \leq 0.07$, two-phase *heterosite* and *olivine* for $0.07 \leq x \leq 0.60$, *olivine* solid solution with vacancies for $0.60 \leq x \leq 0.90$, undetermined phase for $0.90 \leq x < 1.00$ and *olivine* solid solution without vacancies for $1.00 \leq x$.

⁷Li MAS NMR spectra of $\text{Li}_x\text{Mn}_{0.5}\text{Fe}_{0.5}\text{PO}_4$ products were recorded to probe Li^+ in the various environments present (Figure 1b). The spectra show two isotropic resonances, (labeled as *A* and *B*). The exact nature of these distinct environments is the subject of investigation. The presence of transition metals in the structure can lead to very large ⁷Li isotropic shifts due to the Fermi contact interaction mediated by the M-O-Li bonds. In the *olivine* case, an environment rich in Fe^{2+} has led to a signal around -56 ppm³² whereas a coordinating sphere rich in Mn^{2+} results in a positive shift of 70 ppm^{7, 33}. The difference in oxidation state and electronic configuration in *d*-orbitals determine the type of interaction and the sign of the chemical shift where a delocalization mechanism is occurring for the high spin $t_{2g}^3 e_g^2 \text{Mn}^{2+}$ and Fe^{3+} and $t_{2g}^3 e_g^1 \text{Mn}^{3+}$ vs a polarization mechanism for the high spin $t_{2g}^4 e_g^2 \text{Fe}^{2+}$.³⁴ In a bimetallic structure with mixed 2+ and 3+ oxidation states, the contribution of each transition metal has an influence on the resulting signal with respect to their statistical distribution in the six transition metal sites of the first Li^+ coordination sphere (SM Figure S4).

For the fully lithiated structure ($x = 1.11$), we report a broad peak (*A*) at 34 ppm (Figure

1b) which is consistent with the previously reported comparable $\text{LiMn}_{0.6}\text{Fe}_{0.4}\text{PO}_4$ material.⁷ Throughout the first step of the delithiation, the chemical shift of peak *A* increased from 34 to 74 ppm (Figure 1b). This indicates that the remaining Li^+ is located in environments with progressively more Mn^{2+} . In contrast, the shift of peak *A* remains constant for $0.07 \leq x \leq 0.67$, indicating that the environment around these Li^+ ions does not change significantly as expected in a two-phase process. The sharp *B* peak with a chemical shift of -1 ppm (Figure 1b) is smaller than peak *A* but has a significant integrated intensity (SM Figure S7) during the first step of delithiation. We suggest the following potential assignments of the *B* peak: i) diamagnetic impurities insoluble in acetonitrile at the surface of particles ii) Li^+ in a Fe^{3+} -rich environment or iii) Li^+ involved in surface diffusion processes^{35, 36}. In contrast to what has been reported previously⁷, the peak at -1 ppm in the present study is not more prominent at the end-of-charge. This may be explained by differences in sample preparation. The fact that a Li^+ miscibility of 3% exists in the Li-poor phase³⁷ did not impact the chemical shift of peaks *A* and *B* considering the convolution of signals from every Li^+ environment but could explain the changes in their relative intensity ratios (SM Figure S7). The material with a very low concentration of Li^+ , *i.e.* $x = 0.07$, entailing low signal strength, exhibits a small peak around 74 ppm with no detectable peak at -1 ppm reinforcing the hypothesis that the 74 ppm peak also contains a signal from Li^+ ions trapped in the bulk structure due to anti-site defects.

Diffusion of Li^+ in the solid $\text{LiMn}_y\text{Fe}_{1-y}\text{PO}_4$ particles is likely to occur preferably in the *b* direction as is the case in LiFePO_4 ³⁸. Probing Li^+ dynamics in paramagnetic battery materials is challenging, but insight can be gained using MAS NMR transverse relaxation (T_2) relaxation measurements²⁸. T_2 relaxation reflects the decrease in transverse magnetization due to the loss of phase coherence between spins, which results from inhomogeneities or fluctuations in the local magnetic field. Herein are the main mechanisms that can cause the loss of spin alignment: i) magnetic field inhomogeneity in the sample or ii) fluctuations of the local magnetic field, caused either by motional effects or electronic fluctuations. The magnetic field inhomogeneities can be considered to have a negligible linewidth contribution in this specific case considering the broadness of ^7Li signal in $\text{LiMn}_y\text{Fe}_{1-y}\text{PO}_4$. Generally, electronic fluctuations are occurring fast compared to the NMR timescale³⁹, T_2 measurements should therefore be dominated by the relatively low frequency processes associated with Li^+ motion. This was confirmed experimentally as detailed below.

First, evolution between T_1 and T_2 values were compared over samples with two different degrees of lithiation (SM Figure S6) to evaluate the impact of change in oxidation state of the transition metals, as presented initially by Zhou *et al.*²⁸. T_1 , also referred as longitudinal relaxation, is affected through a process where the absorbed energy by the nuclei is dissipated *via* the lattice for the return to equilibrium. T_1 is more sensitive to high frequency processes⁴⁰, *e.g.* electron hopping, and a change in oxidation state from M^{2+} to M^{3+} ($\text{M} = \text{Mn}$ or Fe) causes an important increase in T_1 . In contrast, T_2 decreases with the amount of mixed valance *M* (SM Figure S6). This opposite behavior suggests that electron effects, that have an important impact on T_1 (SM Figure S6) are not the dominating source for changes in T_2 .

Secondly, considering the complex relationship of T_2 parameter and Li^+ motion, a prior experiment was executed in order to evaluate if the NMR method was sufficiently sensitive to detect Li^+ hopping occurring at room temperature in these types of materials. T_2 parameters were measured in $\text{Li}_x\text{Mn}_{0.7}\text{Fe}_{0.3}\text{PO}_4$ (for $x = 0.83$ and $x = 1.08$) as a function of sample

temperature (Figure 2). The assignment of peak *A* and *B* (SM Figure S8) is consistent with previous material but the resolution of peak *B* specifically for $\text{Li}_{1.08}\text{Mn}_{0.7}\text{Fe}_{0.3}\text{PO}_4$ is not sufficient to extract a T_2 value. For the sample with no vacancies ($x = 1.08$), there is no significant change in T_2 vs temperature up to $T = 345$ K (Figure 2). This is consistent with negligible motional effects for all atoms within the structure and that the activation energy for Li^+ hopping is significant, as expected for a sample without vacancies. In contrast, the non-zero slope of the linear fit for the bulk *olivine* solid solution sample, *i.e.* $x = 0.83$ (*A*), is notable over the whole temperature range. Atomic motion should unambiguously increase with temperature, usually leading to a faster transverse relaxation and a smaller T_2 value²⁸. Consequently, the lack of T_2 change with temperature in the sample with no vacancies, compared to the significant change in samples with vacancies strongly suggest that T_2 relaxation is correlated with Li^+ hopping. This is further consistent with the fact that all atoms other than Li^+ are strongly bound within the structure⁴¹. Specifically for the peak *B* of sample $x = 0.83$ and notwithstanding low resolution (SM Figure S8), the invariance of T_2 at low temperature (Figure 2) could indicate that the required activation energy is not reached, consistent with Li^+ in a constrained environment, *e.g.* at the interface between two-phases or at the surface of the particle.

The combined data for peak *A* in each sample show that changes in T_2 is conditional to the presence of vacancies and increase with temperature, therefore the measurement of ^7Li T_2 changes can be employed as an indirect probe of Li^+ hopping in $\text{Li}_x\text{Mn}_y\text{Fe}_{1-y}\text{PO}_4$. Also, the comparison with T_1 show that changes in T_2 are not *predominantly* affected by changes in oxidation states of the transition metals in this specific case, *i.e.* the contribution is not entirely excluded and could be interesting for future work.

The phases identified by Rietveld refinement (SM, Figure S2) at specific states of lithiation coupled with T_2 values gives a representation of the change in Li^+ motion during the charging process of $\text{LiMn}_{0.5}\text{Fe}_{0.5}\text{PO}_4$ (Figure 3a). During delithiation, the initial T_2 value is elevated for the *olivine* structure without vacancies indicating slow transverse relaxation caused by a low Li^+ mobility due to the lack of vacancies. This is followed by an immediate reduction as vacancies offering more “hopping” sites are created in the *olivine* solid solution structure during charging (Figure 3a) (SM Figure S9). Another contribution to this enhanced Li^+ motion is the possible augmentation of the bottleneck area found between three oxygens of the octahedra across Li^+ zigzag path, where the enlargement of this area would facilitate Li^+ hopping due to steric considerations.⁴² A detailed analysis of atomic positions is outside the scope of this paper but a simple comparison of the unit cell volumes for $\text{Li}_{0.55}\text{Mn}_{0.5}\text{Fe}_{0.5}\text{PO}_4$ vs $\text{Li}_{0.67}\text{Mn}_{0.5}\text{Fe}_{0.5}\text{PO}_4$ (SM Table 2) suggests that the Li^+ path within the interface of the two-phase material could suffer from a reduced bottleneck size compared to the *olivine* solid solution with vacancies. Moreover, the two-phase system is associated with an increase in T_2 value (Figure 3a), where Li^+ motion in the bulk of the particle could face limitation in terms of the number of hopping paths available (SM Figure S9). At the end of delithiation, a high T_2 value suggests that the remaining Li^+ motion is hindered due to their anti-site defects nature (Figure 3a).

Turning to peak *B*, a constant T_2 value of 214 ± 11 μs for over every degree of lithiation is measured. Moreover, the *B* peak is present on the ^7Li MAS NMR spectrum of every sample, even in the ones exhibiting a single phase in XRD (Figure 1), possibly because of XRD lower

sensitivity to local changes. The initial suggested assignment of peak *B* to either i) diamagnetic impurities insoluble in acetonitrile at the surface of particles ii) Li^+ in a Fe^{3+} -rich environment or iii) Li^+ involved in surface diffusion processes^{35,36} will be subject of future investigation to determine how this unchanging T_2 value impact Li^+ transport in the rest of the particle.

The synthesis method used in this work provides materials with similar particles size and morphology while various Mn level are incorporated in an *olivine* solid solution as witnessed by the unit cell evolution following Vegard's law (SM Table S2). As such, the impact of Mn inclusion on Li^+ transport can be evaluated over several phases. By combining T_2 values in a two-dimensional phase diagram (Figure 3b), the significant increased motional freedom found in the *olivine* solid solution phases with vacancies is confirmed across different Mn contents. The section where the structure is more likely to be an *olivine* solid solution with vacancies has been represented to comprise identified phases from Rietveld refinement. Herein, the number of samples employed and discrepancies reported from the literature^{14, 15} limit the representation to an approximated zone. For the $\text{Li}_x\text{Mn}_{0.7}\text{Fe}_{0.3}\text{PO}_4$ sample, the transition from *olivine* solid solution to the more oxidized two-phase system yields an increase in T_2 value, as is the case for the $y = 0.5$ composition (Figure 3b). Focusing only on the *olivine* solid solution with vacancies zone for the studied samples, Li^+ motion is maximized for $y \leq 0.5$ but slower for $y = 0.7$. Although the *olivine* solid solution phase with vacancies has structural advantages by reducing structural lattice mismatch within a fixed y , a higher Mn concentration has been associated with a loss of $\text{Mn}^{2+}/\text{Mn}^{3+}$ redox activity and a shift in redox potential.⁵ However, the exact nature of trend is not clear as the kinetics of Fe and Mn have opposite behavior as a function of the Mn content.⁵ Although it is beyond the scope of this paper, *in situ* characterization of such bimetallic structure during oxidation would be relevant to extract a continuous range of Li^+ composition, associated phases and their consequences on Li^+ motion.

Conclusions

Chemically prepared $\text{Li}_x\text{Mn}_y\text{Fe}_{1-y}\text{PO}_4$ with strategic compositions has been characterized using XRD and ^7Li MAS NMR to provide a global picture of the delithiation process. Compared to an electrochemical approach limited by ionic and electronic transport in the electrode, the chemical oxidation employed here is expected to yield more uniform samples. ^7Li MAS NMR T_2 relaxation changes were assigned to Li^+ hopping activity after examining two prerequisites: i) when changing the state of charge of the material, T_1 and T_2 have opposite behavior suggesting electron effects are not dominating T_2 and ii) samples with no vacancies, and therefore limited Li^+ mobility, showed no change in T_2 with temperature distinct from samples with vacancies. Consequently, in the studied $\text{Li}_x\text{Mn}_y\text{Fe}_{1-y}\text{PO}_4$ cases Li^+ motion is a dominant contribution in the fluctuation of the local magnetic field entailing a faster transverse relaxation. For both $y = 0.5$ and $y = 0.7$ samples, *olivine* solid solution phase with vacancies exhibited a faster transverse relaxation due to superior Li^+ motion for each Mn composition. The presence of vacancies, and significantly their random distribution within the structure, favors Li^+ transport. This result reinforces the interest in developing lithium multi-metal structures where the existence of a transient solid solution improved Li^+ transport. The ^7Li MAS NMR method offers many advantages in complement to

electrochemical techniques, *e.g.* GITT or impedance spectroscopy: it focuses on the ion transport within the solid only, thereby eliminating surface chemistry concerns, it informs on the specific ion environment where motion is probed and it does not involve multiple components as in composite electrode. In here, the technique gave access to one of the most fundamental parameters in intercalation materials, bulk Li⁺ transport. As such it holds the potential to become a key tool to guides the development of novel enhanced positive Li-ion battery electrode chemistries.

Acknowledgments

The authors would like to thank Dr. Alexandre A. Arnold (NanoQAM) for his valuable advice and technical assistance in NMR spectroscopy. The authors thankfully acknowledge the Natural Sciences and Engineering Research Council of Canada (NSERC) Grant No. 326937-2013-RGPIN and RGPIN-2019-07200 for financial support as well as Fonds de recherche du Québec – Nature et technologies (FRQNT) for doctoral scholarship No. 287755 (L. Savignac).

References

1. J. Liu, J. Wang, X. Yan, X. Zhang, G. Yang, A. F. Jalbout and R. Wang, *Electrochimica Acta*, **54**, 5656 (2009).
2. V. Srinivasan and J. Newman, *Journal of The Electrochemical Society*, **151**, A1517 (2004).
3. C. Kuss, N. D. Trinh, S. Andjelic, M. Saulnier, E. M. Dufresne, G. Liang and S. B. Schougaard, *The Journal of Physical Chemistry Letters*, **8**, 6160 (2017).
4. N. Nitta, F. Wu, J. T. Lee and G. Yushin, *Materials Today*, **18**, 252 (2015).
5. G. Kobayashi, A. Yamada, S. Nishimura, R. Kanno, Y. Kobayashi, S. Seki, Y. Ohno and H. Miyashiro, *Journal of Power Sources*, **189**, 397 (2009).
6. V. Aravindan, J. Gnanaraj, Y.-S. Lee and S. Madhavi, *Journal of Materials Chemistry A*, **1**, 3518 (2013).
7. I. Bezza, M. Kaus, R. Heinzmann, M. Yavuz, M. Knapp, S. Mangold, S. Doyle, C. P. Grey, H. Ehrenberg, S. Indris and I. Saadoun, *The Journal of Physical Chemistry C*, **119**, 9016 (2015).
8. Y. Huang, J. Fang, F. Omenya, M. O'Shea, N. A. Chernova, R. Zhang, Q. Wang, N. F. Quackenbush, L. F. J. Piper, D. O. Scanlon and M. S. Whittingham, *Journal of Materials Chemistry A*, **2**, 12827 (2014).
9. L. F. J. Piper, N. F. Quackenbush, S. Sallis, D. O. Scanlon, G. W. Watson, K. W. Nam, X. Q. Yang, K. E. Smith, F. Omenya, N. A. Chernova and M. S. Whittingham, *The Journal of Physical Chemistry C*, **117**, 10383 (2013).
10. M. Yonemura, A. Yamada, Y. Takei, N. Sonoyama and R. Kanno, *Journal of the Electrochemical Society*, **151**, A1352 (2004).
11. S. K. Martha, J. Grinblat, O. Haik, E. Zinigrad, T. Drezen, J. H. Miners, I. Exnar, A. Kay, B. Markovsky and D. Aurbach, *Angewandte Chemie International Edition*, **48**, 8559 (2009).
12. J. Lu, G. Oyama, S.-i. Nishimura and A. Yamada, *Chemistry of Materials*, **28**, 1101 (2016).
13. N. Meethong, H.-Y. S. Huang, S. A. Speakman, W. C. Carter and Y.-M. Chiang, *Advanced Functional Materials*, **17**, 1115 (2007).
14. N. D. Trinh, Les batteries lithium-ion à haute densité énergétique : nouvelle formulation et

caractérisation de matériaux d'insertion substitués pour l'électrode positive, in, Université du Québec à Montréal, Montréal (2016).

15. S. Loftager, S. B. Schougaard, T. Vegge and J. M. García-Lastra, *The Journal of Physical Chemistry C*, **123**, 102 (2019).

16. A. Yamada, Y. Kudo and K.-Y. Liu, *Journal of The Electrochemical Society*, **148**, A1153 (2001).

17. A. Perea, M. T. Sougrati, C. M. Ionica-Bousquet, B. Fraisse, C. Tessier, L. Aldon and J.-C. Jumas, *RSC Advances*, **2**, 2080 (2012).

18. Y.-C. Chen, J.-M. Chen, C.-H. Hsu, J.-W. Yeh, H. C. Shih, Y.-S. Chang and H.-S. Sheu, *Journal of Power Sources*, **189**, 790 (2009).

19. N. N. Bramnik, K. G. Bramnik, K. Nikolowski, M. Hinterstein, C. Baetz and H. Ehrenberg, *Electrochemical and Solid State Letters*, **8**, A379 (2005).

20. N. D. Trinh, Z. W. Ai, G. Liang and S. B. Schougaard, *Solid State Ionics*, **324**, 33 (2018).

21. S. Wi, J. Park, S. Lee, J. Kim, B. Gil, A. J. Yun, Y.-E. Sung, B. Park and C. Kim, *Nano Energy*, **39**, 371 (2017).

22. O. A. Drozhzhin, V. D. Sumanov, O. M. Karakulina, A. M. Abakumov, J. Hadermann, A. N. Baranov, K. J. Stevenson and E. V. Antipov, *Electrochimica Acta*, **191**, 149 (2016).

23. D. B. Ravnsbæk, K. Xiang, W. Xing, O. Borkiewicz, K. Wiaderek, P. Gionet, K. Chapman, P. Chupas and Y.-M. Chiang, *Nano letters*, **14**, 1484 (2014).

24. K.-W. Nam, W.-S. Yoon, K. Zaghbi, K. Y. Chung and X.-Q. Yang, *Electrochemistry communications*, **11**, 2023 (2009).

25. S.-W. Kim, J. Kim, H. Gwon and K. Kang, *Journal of The Electrochemical Society*, **156**, A635 (2009).

26. H. Liu, M.-J. Choe, R. A. Enrique, B. Orvañanos, L. Zhou, T. Liu, K. Thornton and C. P. Grey, *The Journal of Physical Chemistry C*, **121**, 12025 (2017).

27. A. R. Wizansky, P. E. Rauch and F. J. Disalvo, *Journal of Solid State Chemistry*, **81**, 203 (1989).

28. L. Zhou, M. Leskes, T. Liu and C. P. Grey, *Angewandte Chemie International Edition*, **54**, 14782 (2015).

29. J. Rodríguez-Carvajal, *Physica B: Condensed Matter*, **192**, 55 (1993).

30. A. L. Van Geet, *Analytical Chemistry*, **42**, 679 (1970).

31. D. Y. W. Yu, K. Donoue, T. Kadohata, T. Murata, S. Matsuta and S. Fujitani, *Journal of The Electrochemical Society*, **155**, A526 (2008).

32. J. Cabana, J. Shirakawa, G. Chen, T. J. Richardson and C. P. Grey, *Chemistry of Materials*, **22**, 1249 (2010).

33. M. C. Tucker, M. M. Doeff, T. J. Richardson, R. Fiñones, J. A. Reimer and E. J. Cairns, *Electrochemical and Solid-State Letters*, **5**, A95 (2002).

34. D. Carlier, M. Ménétrier, C. P. Grey, C. Delmas and G. Ceder, *Physical Review B*, **67**, 174103 (2003).

35. Y. Li, H. Chen, K. Lim, H. D. Deng, J. Lim, D. Fraggedakis, P. M. Attia, S. C. Lee, N. Jin, J. Moškon, Z. Guan, W. E. Gent, J. Hong, Y.-S. Yu, M. Gaberšček, M. S. Islam, M. Z. Bazant and W. C. Chueh, *Nature Materials*, **17**, 915 (2018).

36. L. Savignac, J. M. Griffin and S. B. Schougaard, *The Journal of Physical Chemistry C*, **124**, 7608 (2020).

37. A. Yamada, H. Koizumi, N. Sonoyama and R. Kanno, *Electrochemical and Solid-State Letters*, **8**, A409 (2005).
38. S.-i. Nishimura, G. Kobayashi, K. Ohoyama, R. Kanno, M. Yashima and A. Yamada, *Nature Materials*, **7**, 707 (2008).
39. D. C. Apperley, R. K. Harris and P. Hodgkinson, *Solid-state NMR: Basic principles and practice*, Momentum Press (2012).
40. J. Cavanagh, W. J. Fairbrother, A. G. Palmer III and N. J. Skelton, *Protein NMR spectroscopy: principles and practice*, Elsevier (1995).
41. C. M. Burba and R. Frech, *Journal of power sources*, **172**, 870 (2007).
42. T. Nakamura, K. Sakumoto, M. Okamoto, S. Seki, Y. Kobayashi, T. Takeuchi, M. Tabuchi and Y. Yamada, *Journal of Power Sources*, **174**, 435 (2007).

Figures

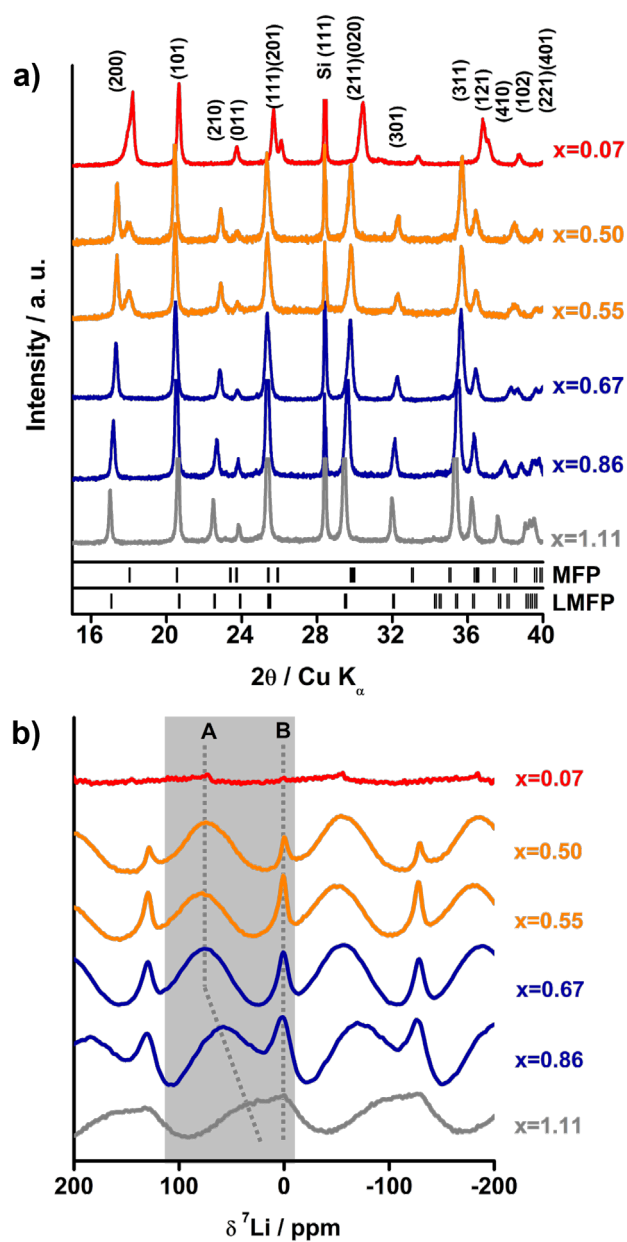


Figure 1. a) Diffractograms of $\text{Li}_x\text{Mn}_{0.5}\text{Fe}_{0.5}\text{PO}_4$ at various x incl. Bragg reflection positions of the lattices for $x = 1$ (LMFP) and $x = 0$ (MFP). b) ^7Li spectra of $\text{Li}_x\text{Mn}_{0.5}\text{Fe}_{0.5}\text{PO}_4$ at various x , peaks that are not rotation band are highlighted in grey and labeled as *A* and *B*. Structure types are color coded *heterosite*: red, *phase separated*: orange, *olivine* solid solution with vacancies: blue and *olivine* without vacancies: grey.

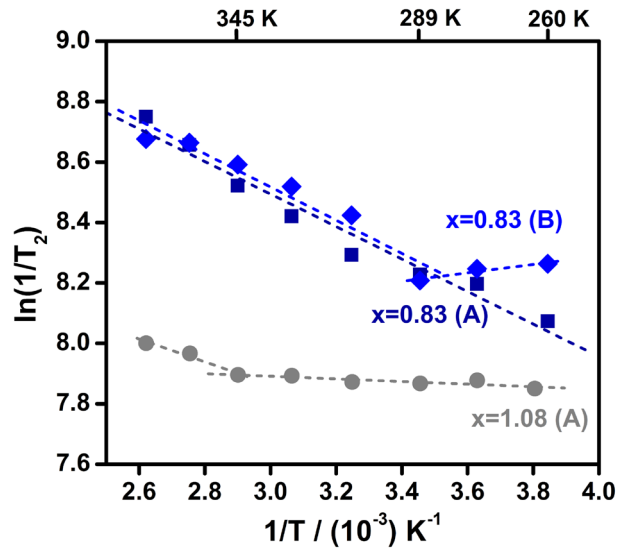


Figure 2. T_2 values at various temperatures for *A* and *B* peaks of $\text{Li}_x\text{Mn}_{0.7}\text{Fe}_{0.3}\text{PO}_4$ with $x = 0.83$ and $x = 1.11$ and their respective linear fit.

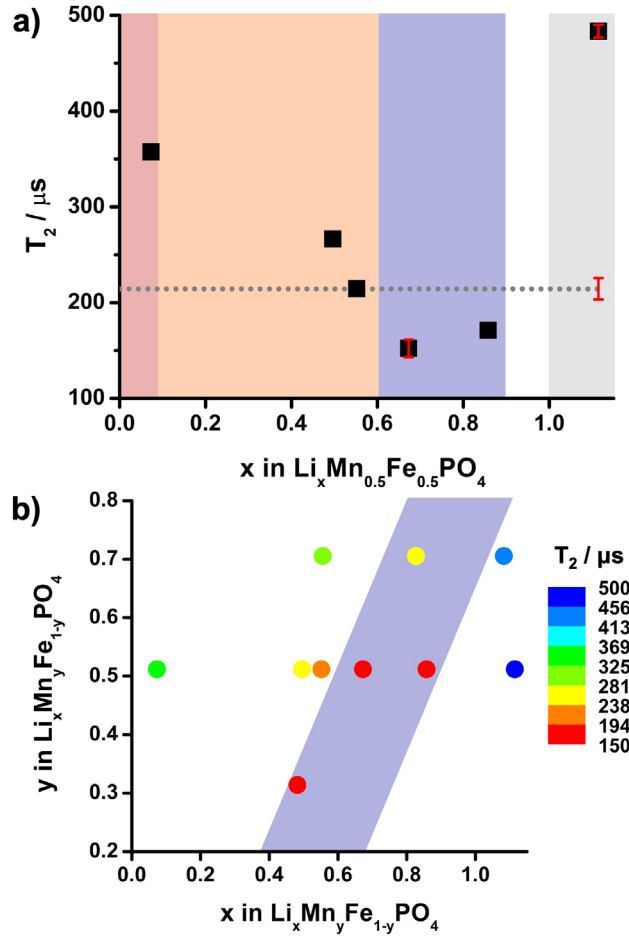


Figure 3. a) T_2 values from peak A (square points) and peak B (dotted line) for $\text{Li}_x\text{Mn}_{0.5}\text{Fe}_{0.5}\text{PO}_4$ at different Li^+ compositions. A red error bar represents the confidence interval. Present phases are indicated in colored zones: *heterosite* (red), phase separation (orange), *olivine* solid solution with vacancies (blue), undetermined phase (white) and *olivine* without vacancies (grey). b) Color-coded plot for $\text{Li}_x\text{Mn}_y\text{Fe}_{1-y}\text{PO}_4$ showing T_2 values from peak A as a function of y and x . The blue section is where the structure is more likely to be an *olivine* solid solution with vacancies.